Bistability in a Superconducting Al Thin Film Induced by Arrays of Fe-Nanodot Magnetic Vortices

J. E. Villegas, C.-P. Li, and Ivan K. Schuller

Physics Department, University of California-San Diego, La Jolla California 92093-0319, USA

(Received 15 January 2007; published 28 November 2007)

A hybrid system, consisting of an array of Fe nanodots covered by a superconducting Al thin film, exhibits very unusual magnetotransport, including a giant hysteretic magnetoresistance with different reversible or irreversible regimes related to the magnetic state of the array. These effects originate from the magnetic fields produced by magnetic nanodots in the "magnetic vortex state." This is a unique model system in which properties of a magnetic array are transferred into the superconductor.

DOI: 10.1103/PhysRevLett.99.227001 PACS numbers: 74.78.Na, 75.47.−m, 75.75.+a

Artificial superconducting/ferromagnetic (S/F) hybrid systems [1] exhibit a vast variety of interesting effects, including proximity [2], collective superconducting pinning [3], domain-wall [4], field-induced [5–7], and spatially modulated superconductivity [8]. In this Letter we investigate a novel S/F structure in which ferromagnetic characteristics are dramatically imprinted into the transport properties of a superconductor (Al) by magnetic fields from a dense magnetic (Fe) nanodot array. The unusual effects reported here are produced by nucleation, displacement and annihilation of magnetic vortices in the nanodots [9–14]. In these the magnetization curls *in plane* around a magnetic vortex core [15], where it points up or down *out of plane* ("vortex polarity"). It is crucial that these magnetic vortices can easily be manipulated with an in-plane applied field comparable to the superconducting critical fields.

This system shows truly hybridized properties (hysteresis and remanence) as properties of magnetic vortices are imprinted into the superconductor. Below T_c the magnetotransport is bistable and can be switched between high- and low-resistance states by the magnetic state of the dots. The high-resistance state is irreversible while the low-resistance one is reversible within certain field limits. The transition between both is controlled by the distribution of vortex polarities in the array. These novel properties induced in the superconductor lead to a giant, remanent, hysteretic magnetoresistance of up to $10^5\%$, in excess of that produced by spin-switch effects [16]. Extensions of this S/F system are ideal to study problems related to percolation, reverse-domain superconductivity [4], etc.

Fe dot (20 nm thick, polycrystalline) arrays covered with a Au protective layer (1 nm thick) were fabricated on Si substrates using nanoporous alumina masks and e-beam evaporation [17]. Scanning electron microscopy (SEM) of the arrays [Fig. 1(a)] exhibits short-range sixfold symmetry [Fig. 1(b)] with typical correlation lengths $\sim 2d - 3d$ (with d the interdot distance) [18], and Gaussian distributions of dot diameters $\varnothing$ [Fig. 1(c)]. We studied three arrays A ($\varnothing = 55 \pm 5$ nm, $d = 85 \pm 20$ nm), B ($\varnothing = 75 \pm 5$ nm, $d = 120 \pm 20$ nm), and C ($\varnothing = 140 \pm 20$ nm, $d = 180 \pm 40$ nm) covered with a superconducting Al thin film of nominal thickness either 20 nm (samples $A20$, $B20$, $C20$) or 40 nm ($A40$, $B40$, $C40$). Atomic force microscopy showed that Al films are strongly corrugated but continuous. A standard four-probe bridge was used for magnetotransport and magnetization was obtained from SQUID magnetometry, with the magnetic field applied *in-plane*. All samples showed similar $T_c = 1.40 \pm 0.02$ K. Upper critical fields H_{c2} obtained from magnetotransport imply a superconducting coherence length $\xi(0) \approx 45$ nm. The penetration depth $\lambda(0) \approx 250$ nm, estimated [19] from T_c and the resistivity $\rho_{4.2\ \mathrm{K}} = 6\ \mu\Omega\,\mathrm{cm}$ give $\kappa(0) = \lambda(0)/\xi(0) \approx 5.5$; i.e., the Al films studied here are type-II superconductors.

The in-plane hysteresis loops $M_{||}(H)$ at $T = 6$ K for $A20$ and $C20$ are shown in Figs. 2(a) and 2(b), respectively. Figures 2(c) and 2(d) show their magnetoresistance at $T = 1.25\ K = 0.89T_c$, with the current J injected parallel to the field. These results are independent of the relative direction between the applied field and J, which rules out field-

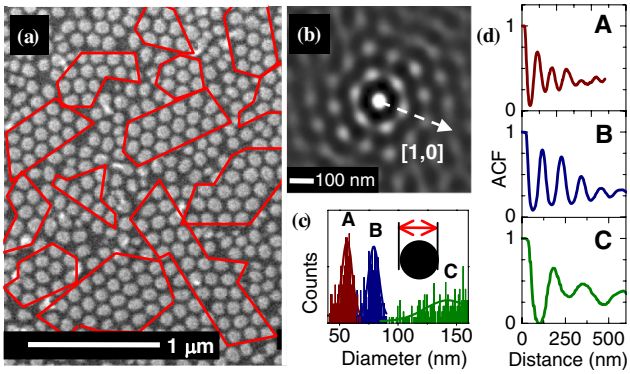

FIG. 1 (color online). (a) SEM image of array B (polygons delimit ordered domains). (b) Autocorrelation function (ACF) for array B. (d) Distribution of dot diameters of arrays A, B, and C. (c) ACF profiles along the [1,0] direction of arrays A, B, and C.

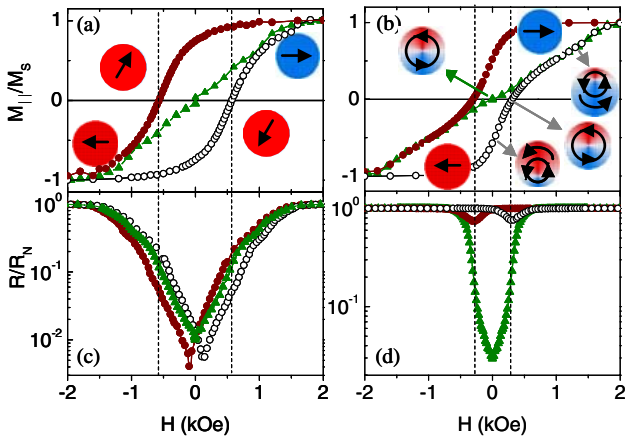

FIG. 2 (color online). (a) Normalized magnetization (M_S saturation magnetization) vs *in-plane* applied field for sample $A20$ at $T = 6$ K. (b) for sample $C20$. (c) Normalized resistance (R_N normal-state resistance) vs *in-plane* applied field for sample $A20$, at $T = 1.25$ $K = 0.89T_c$ with $J = 25$ kA cm^{-2}. (d) For sample $C20$. Hollow (white) and solid (brown) dots for curves measured from negative and positive saturation, respectively. Triangles (green) for virgin curves. Negative branches of $M_{||}(H)$ virgin curves are mirrored from positive ones. Vertical lines point out coercive fields. The sketches are a cartoon of the reversal mechanisms.

induced flux dynamics as the origin of the observed effects. $M_{||}(H)$ of the dot array is essentially the same at $T = 6$ K and $T = 1.25$ K (i.e., above and below T_c) since the temperature dependence of the magnetization is saturated. Moreover, since the Al thickness is much smaller than $\lambda(0.89T_c) \approx 550$ nm, the in-plane external field penetrates through the film and its diamagnetic response can be neglected [19]. The solid (brown) and hollow (white) data are measured from positive to negative saturation ($H_S \rightarrow -H_S$, with $H_S \approx 2.5$ kOe) and vice versa, respectively. Triangles (green) are for the ''virgin'' curves. Before these, the sample was demagnetized with an ac magnetic field of decreasing amplitude. Then, measurements were performed from zero magnetization to positive (negative) saturation ($0 \rightarrow \pm H_S$).

The hysteresis loop [Fig. 2(a)] of array A is as expected for single magnetic domain dots [13] and reversal via magnetization rotation (see sketches). Arrays B or C [$C20$ shown in Fig. 2(b)] behave differently from A: there is a characteristic ''pinching'' in middle of the loop, reduced coercivity ($H_C = 0.575$, 0.375, and 0.275 kOe for A, B, and C, respectively) and remanence ($0.75M_S$, $0.35M_S$, and $0.45M_S$), and a virgin curve that quickly merges into the major loop. These are distinctive features of vortex-state mediated magnetization reversal, as we found earlier [12,13] and showed by neutron diffraction [14]. A cartoon of this reversal mechanism is depicted in Fig. 2(b); from negative to positive saturation (coded red to blue), the three main consecutive events are vortex nucleation ($H_n \approx -100$ Oe [13]), displacement of the vortex-core to the center of the dot (at H_C), and vortex annihilation ($H_a \approx$ 1.5–1.25 kOe for arrays B-C). Because of the imperfections in these arrays there is a distribution of annihilation or nucleation fields, with full-width at half-maximum $\sim$0.5 kOe [13] (the mean annihilation or nucleation fields are discussed below). Dipolar interactions between nanodots are not negligible since $d < 2\varnothing$ [12].

Sample $A20$ exhibits a magnetoresistance [Fig. 2(c)] similar when the field is swept from positive to negative saturation $H_S \rightarrow -H_S$ (or vice versa) or when swept from zero field to saturation $0 \rightarrow H_S$ after a demagnetizing cycle. For lower fields, a decrease of several orders of magnitude in resistance characterizes the transition into the superconducting state. Curves measured from positive (negative) saturation shift towards negative (positive) fields with a minimum resistance at $\sim \mp 60$ Oe. In contrast, the virgin curve is symmetric around $H = 0$ Oe. This shift originates from the external field compensation [6] by the remanent magnetization of the dot array.

Samples with arrays B and C (vortex-state) exhibit a radically different behavior [see Fig. 2(d)] for $C20$. This is the main result of our Letter. When the field is swept from positive (or negative) saturation $H_S \rightarrow -H_S$ the resistance remains close to normal-state values, with small minima (at $H \sim 0.5$ and $\sim$0.3 kOe for B and C respectively) around the coercive fields. After a demagnetizing cycle, a deep superconducting transition takes place at low fields. Depending on the magnetic history, two different resistances high (R_h) and low (R_l) are found for a fixed applied magnetic field in a certain range. Interestingly, typical ferromagnetic properties, hysteresis and remanence, are dramatically imprinted into the magnetotransport. This induces a current (J) dependent giant, remanent, hysteretic magnetoresistance $(R_h - R_l)/R_l$ as large as $10^5\%$ at *zero applied field*. Even the more subtle magnetic behavior characteristic of nanodots in the vortex-state is transferred to the transport properties. Arrays B and C exhibit a linear, *reversible* response near the origin in the virgin $M_{||}(H)$ curve [triangles in Fig. 2(b)]. This is due to the reversible vortex-core motion within the nanodots [13]. After the low-resistance state is established by a demagnetizing cycle [triangles in Fig. 2(d)], $R(H)$ is also reversible and is constant as the field is swept back and forth. Reversibility is lost and remanence is observed [in $R(H)$ and $M_{||}(H)$] after the applied field exceeds $\sim$1.5 and $\sim$1.25 kOe for arrays B and C, respectively. The vortex annihilation field gives this threshold field.

Figure 3 shows the switching between the low- and high-resistance states for sample $B20$. After applying a positive saturating field H_S, $R(H)$ was measured as the field was decreased to a field $H_R \leq 0$ and then swept back to positive saturation ($H_S \rightarrow H_R \rightarrow H_S$; minor loops). $M_{||}(H)$ cycles were independently measured (not shown). Cycles with $|H_R| \approx$ 1–1.25 kOe lead to the low-resistance state, while

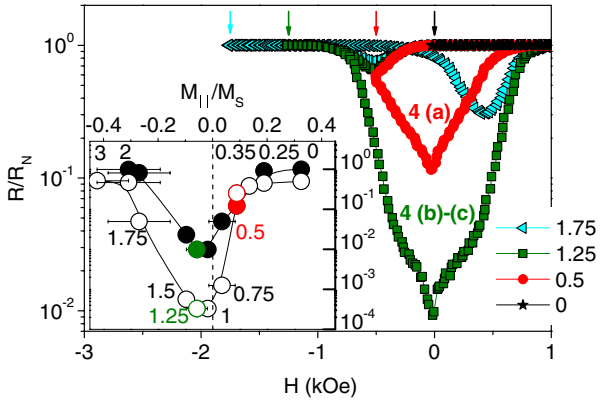

FIG. 3 (color online). Normalized resistance vs in-plane applied field of sample $B20$ at $T = 1.25\ K = 0.89T_c$ with $J = 25\ \mathrm{kA \cdot cm^{-2}}$ (R_N normal-state resistance) for cycles with different $|H_R|$ (see text). Arrows point out H_R, legend in kOe. The labels 4 (a) and 4 (b)–(c) point to the corresponding situations in Fig. 4. Inset: Normalized resistance vs. normalized *in-plane* magnetization (M_S saturation magnetization) at *zero applied field*. Solid (hollow) circles for samples $B20$ ($B40$). Each point corresponds to a $|H_R|$ indicated by the numbers close to each point. Lines are guides to the eye.

those with larger or smaller $|H_R|$ lead to the high-resistance one. Using $R(H)$ and $M_{||}(H)$ we obtained $R(M_{||})$ for any field H. $R(M_{||})$ at zero applied magnetic field $H = 0$ helps clarify the role of the dots' magnetic state for this unusual behavior (see inset of Fig. 3, the labels indicate $|H_R|$). All the samples with dots in the vortex state behave qualitatively the same.

The in-plane magnetization $|M_{||}/M_S| > \sim 0.4$ drives the sample into the normal state independently of the magnetic history. However, $M_{||}$ cannot account by itself for the switching between the different states in Fig. 3. The inset of this figure shows a strong asymmetry $R(M_{||}) \neq R(-M_{||})$ (note the logarithmic scale) around $|M_{||}/M_S| \approx 0.05$–$0.15$, with $R(-M_{||})$ 2 to 4 orders of magnitude lower than $R(M_{||})$. This implies that besides the in-plane magnetization $M_{||}$ an additional "hidden" variable (*linked to the magnetic history*) leads to this behavior. The only neglected magnetic variable is the out-of-plane magnetization $M_\perp$ in the vortex cores, which must play a significant role. Note (see labels in the inset of Fig. 3) that the low-resistance state is achieved in cycles with $|H_R| =$ 1–15 kOe ($|H_R| = 0.75$–1.25 kOe for array C, not shown). These fields, close to the vortex annihilation fields found in these arrays [13], qualitatively follow the expected trend (the annihilation fields scale with dot size) [10]. Thus the high to low-resistance transition is triggered as the applied field is cycled around the annihilation fields, and is connected to $M_\perp$ in the vortex cores. Other mechanisms such as proximity effects [2] are ruled out by similar observations in samples where the transparency of the Fe/Al interfaces was reduced by an FeO_x layer.

To evaluate the effect of $M_\perp$ on the superconducting film we calculated the out-of-plane magnetic field $H_\perp$ produced by the vortex cores [20] and compared it to the superconducting critical field H_{Cr} [22]. The magnetic field profiles obtained are strongly dependant on the distribution of vortex polarities. Figure 4 shows $H_\perp(x, y)$ (with x, y the in-plane coordinates) for array B, in which (a) all the vortices have the same polarity, (b) random distribution of polarities, and (c) an antiferromagnetic (AF) arrangement of polarities. White areas in Fig. 4 correspond to regions with $H_\perp < H_{\mathrm{Cr}} \approx 20$ Oe. Superconductivity is locally suppressed on top of the magnetic dots because there $H_\perp > H_{\mathrm{Cr}}$ regardless of the polarity distribution. Thus, the system shows *zero* resistance if the supercurrent percolates along areas between the dots where $H_\perp < H_{\mathrm{Cr}}$. This is similar to percolation in a hexagonal network, for which the percolation threshold (minimum percentage of conducting bonds for a conducting network) is 33% [23]. If all the vortices have the same polarity [Fig. 4(a)], $H_\perp > H_{\mathrm{Cr}}$ everywhere and the Al film is expected to be in the normal state. With a random distribution of polarities [Fig. 4(b)], $H_\perp > H_{\mathrm{Cr}}$ in between vortices with opposite polarity ($\sim$20% of the space between dots) and, even if not enough to allow complete percolation, a lower *finite* resistance is expected. Finally, for an AF distribution [Fig. 4(c)] $H_\perp > H_{\mathrm{Cr}}$ in $\sim$36% of the space between dots, and therefore percolation and *zero* resistance is expected. Figure 4 should not be taken literally as the situations in real samples. The actual arrays present short-range order and many possible degenerate ground states similar to Fig. 4(c). Moreover, the vortex cores are not pinned in the center of the dots. However, these calculations show that a high- to low-resistance transition is expected as the polarity distribution changes from one with the same polarity for the majority of vortices to other in which 50% of the vortices point up or down. Evidence is found if a 10 kOe positive field applied out-of-plane (well above the coercive field $H_C \approx 1.5$ kOe) induced the same polarity [9] in all magnetic vortices. As expected from Fig. 4(a) removal of that field did not restore the superconducting state. This

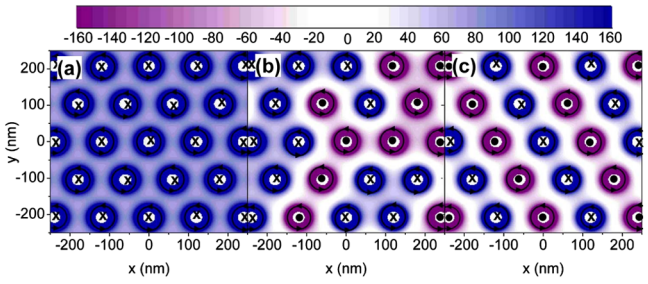

FIG. 4 (color online). Calculated out-of-plane field $H_\perp(x, y)$ produced by the vortex cores of array B (see color grade legend in Oe), for a (a) distribution with all vortices having the same polarity, (b) random distribution of polarities and (c) AF distribution.

could be recovered either by the application of a positive out-of-plane external field $H \approx 25$ Oe that compensates the magnetic field from the vortex cores, or a demagnetizing cycle to restore a balanced vortex polarity distribution (50% up or down). This discussion also applies to array *C*, except that two vortex cores might be present in these larger dots.

The superconducting to normal phase boundary is controlled by the combined effects of the applied field, the in-plane and out-of-plane magnetization in the vortex cores. The latter has two effects. On the one hand, it suppresses superconductivity on top of the dots. Since superconductivity nucleates only in *between* the dots, the *in-plane* magnetization has a stronger effect than with arrays of single magnetic domain dots (*A*). On the other hand, nucleation of superconductivity between the dots is strongly affected by the vortex polarity distribution, causing high- or low-resistance for similar in-plane magnetizations. The minor loops in Fig. 3 arise from the fact that (i) the polarity of a single vortex is set at nucleation and annihilation/renucleation is required to change it, and (ii) there is a finite distribution of annihilation or nucleation fields [13]. The high-resistance observed as the external field is reduced from saturation ($H_S \rightarrow H$) implies that a majority of vortices nucleate with equal polarity [Fig. 4(a)]. Although this is in principle unexpected (a 50% up or down polarity distribution is energetically favorable), it can be caused by the unavoidable misalignments between the applied field and the array plane, as shown by micromagnetic simulations in which $\sim 4°$ misalignment produces 85% of the vortices to have same polarity. The low-resistance implies a balanced population of polarities (50% up or down). It is observed after the field is reduced further to H_R at which only a fraction of the vortices are annihilated, and then reversed ($H_S \rightarrow H_R \rightarrow H$, Fig. 3). Vortices annihilated at H_R renucleate with opposite polarity, to reduce magnetostatic interactions with their neighbors and due to the external field misalignment that now favors the opposite polarity. This cycle yields a balanced population of polarities [Figs. 4(b) and 4(c)]. Since the polarity distributions only change through annihilation or nucleation processes, the low-resistance state is reversible as long as the applied field is below the annihilation field of most vortices. A visualization technique such as magnetic force microscopy would be desirable to verify the vortex polarity distributions suggested above. However, unlike for larger vortex cores [9], the small vortex cores here ($\sim$15 nm [11,14]) are close or below the resolution of this technique.

In summary, we have shown that the properties of magnetic vortices can be *imprinted* into the transport properties of superconducting (Al) thin films. This modifies dramatically the behavior of the superconductor, inducing a very unusual hysteretic, remanent magnetoresistance, and different regimes in which magnetoresistance and magnetization show simultaneously reversible or irreversible behavior. These effects are induced by magnetic fields produced by the magnetic dots, and are expected to fade away at temperatures further below T_c as critical fields increase.

Work supported by NSF and AFOSR. J. E. V. acknowledges support from the Spanish MEC. We thank J. L. Vicent, X. Batlle, J. Santamaría, and C. Miller for useful discussions.

[1] I. Schuller, R. Orbach, and P. M. Chaikin, Phys. Rev. Lett. **41**, 1413 (1978).
[2] A. I. Buzdin, Rev. Mod. Phys. **77**, 935 (2005).
[3] J. E. Villegas *et al.*, Phys. Rev. Lett. **97**, 027002 (2006).
[4] J. Fritzsche *et al.*, Phys. Rev. Lett. **96**, 247003 (2006).
[5] L. F. Lyuksyutov and V. L. Pokrovsky, Phys. Rev. Lett. **81**, 2344 (1998).
[6] M. Lange *et al.*, Phys. Rev. Lett. **90**, 197006 (2003).
[7] M. V. Milosevic and F. M. Peeters, Phys. Rev. Lett. **93**, 267006 (2004).
[8] D. Stamopoulos, M. Pissas, and E. Manios, Phys. Rev. B **71**, 014522 (2005).
[9] T. Shinjo *et al.*, Science **289**, 930 (2000).
[10] K. Guslienko *et al.*, Phys. Rev. B **65**, 024414 (2001).
[11] A. A. Wachowiak *et al.*, Science **298**, 577 (2002).
[12] J. Mejía-López *et al.*, J. Appl. Phys. **100**, 104319 (2006).
[13] R. K. Dumas, Phys. Rev. B **75**, 134405 (2007).
[14] I. V. Roshchin *et al.* (unpublished).
[15] Magnetic vortices must not be confused with Abrikosov vortices.
[16] V. Peña *et al.*, Phys. Rev. Lett. **94**, 057002 (2005).
[17] C.-P. Li *et al.*, J. Appl. Phys. **100**, 074318 (2006).
[18] Correlation length is the distance over which the amplitude of the autocorrelation function (ACF) decays to 37%. $\mathrm{ACF}(x, y) \propto \iint I(\alpha, \beta) I(x + \alpha, y + \beta) d\alpha d\beta$ obtained from SEM images $I(\alpha, \beta)$ of the arrays.
[19] M. Tinkham, *Introduction to Superconductivity* (McGraw-Hill, New York, 1975).
[20] We used $M_\perp[r] = M_s(\Theta[1 - r] + \Theta[r - 1] \times (s + 1 - r)/s)$ for the magnetization in the vortex cores, with $r \leq 10$ nm the distance from its center, $\Theta[x]$ the Heavyside's step function, $M_s = 1.65$ kOe the Fe saturation magnetization and $s = 8.97 \pm 0.13$ obtained from fitting to experimental data [11]. $H_\perp(x, y)$ at the film plane calculated using magnetostatics [21] for a 9×9 hexagonal array.
[21] J. D. Jackson, *Classical Electrodynamics* (John Wiley & Sons, New York, 1962).
[22] The Abrikosov vortices size $\sim 2\xi$, ($\xi[0.89T_C] \approx 150$ mm) is larger than the distance between magnetic vortex cores. Due to this constraint, the superconductor is directly driven from the Meissner into the normal state if the field from the vortex cores is strong enough [7]. Therefore, we compared it to the thermodynamic critical field $H_{\mathrm{Cr}} = \lambda^{-1}(H_{c2}\phi_0/4\pi)^{1/2}$ [19]. Since for *B*20 the *out-of-plane* $H_{c2}(0.89T_c) \approx 100$ Oe we estimate $H_{\mathrm{Cr}}(0.89T_c) \approx 20$ Oe.
[23] M. B. Isichenko, Rev. Mod. Phys. **64**, 961 (1992).